RESEARCH REPORT

VTT-R-07064-10

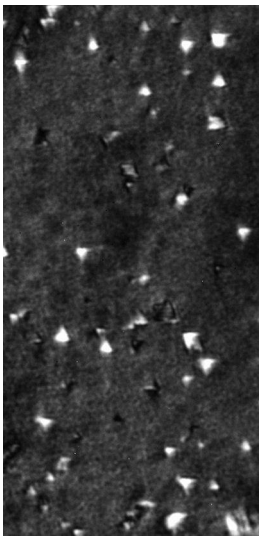

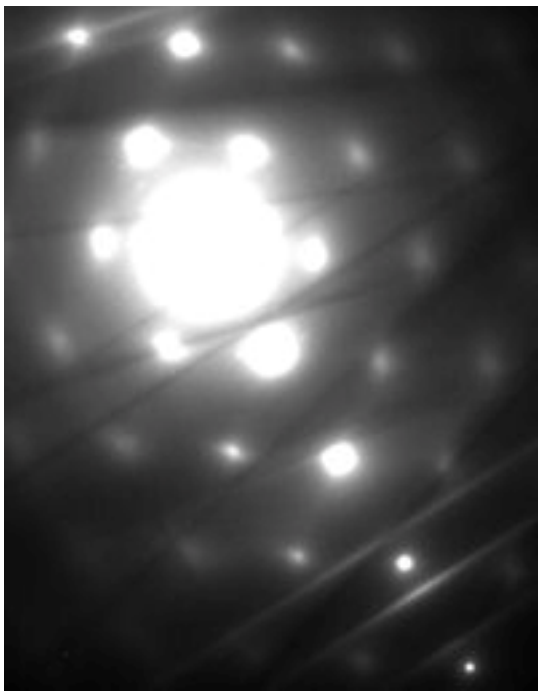

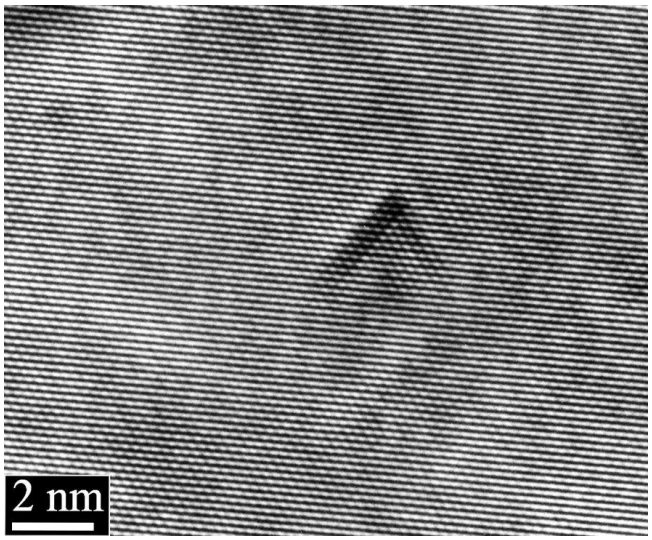

Quantitative analysis of irradiation defects of in-reactor tested copper by weak beam method in TEM

Authors: Janne Pakarinen

Confidentiality: Public

Report's title	
Quantitative analysis of irradiation defects of in-reactor tested copper by weak beam method in TEM	
Customer, contact person, address European Fusion Development Agreement EFDA CSU	Order reference TW5-TVV-SITU2
Project name FU-MAT 10	Project number/Short name 70870
Author(s) Janne Pakarinen	Pages 18/
Keywords TEM, in-reactor tensile testing, irradiation defects, weak beam imaging	Report identification code VTT-R-07064-10

Summary

In this study, the main physical principles of the weak beam dark field (WBDF) method in transmission electron microscopy (TEM) are reviewed, and four neutron irradiated copper samples from in-reactor tensile tests are investigated. Neutron irradiation changes the mechanical behaviour of materials, which needs to be taken into consideration both in current nuclear power plants as well as the fusion-based plants of the future.

Due to the physical properties of copper, ~90 % of the irradiation damages are stacking fault tetrahedra (SFT). The SFT sizes usually range from 1 to 5 nm, which makes the quantitative analysis of them challenging by any method. WBDF has been developed to investigate small centers of strain, and therefore it is well suited for the analysis of SFT.

As a main result it was found that the irradiation doses from 0.01 to 0.04 dpa created SFT densities from 3.6 to 5.2 × 10^{23} SFT/m^3. The results for the materials of this study were in line with observations reported in the literature.

Confidentiality	Public

Espoo 16.12.2010

Written by	Reviewed by	Accepted by
Janne Pakarinen, Research Scientist	Seppo Tähtinen Senior Research Scientist	Pentti Kauppinen Technology Manager

VTT's contact address
Kemistintie 3, P.O. Box 1000, FI-02044 VTT

Distribution (customer and VTT)

Preface

This report is a part of the work carried out in Associations Euratom-Tekes by VTT Materials for Power Engineering under the Task TW5-TVV-SITU2 *In-situ Investigation of the Mechanical Performance and Life Time of Copper*.

Contents

1 Introduction

Irradiation of metals causes an increase in their yield stress and a decrease in their ductility, as shown in Fig. 1. The degradation of materials properties needs to be taken into consideration both in current fission nuclear power plants as well as for the fusion-based plants of the future. The mechanical instability is believed to originate from a localized plastic flow associated with cascade-induced source hardening (CISH). According to three-dimensional dislocation dynamics simulations, the origin of 100 - 200 nm wide defect-free channels, where the plastic strain localizes, is shown to be the defect-dislocation interactions (pinning, unpinning, absorption of defects, etc.) [1].

Neutron impact creates a collision cascade of displacement atoms that causes the damage. A large number of different radiation damages have been identified, for example, dislocation loops, voids, and stacking fault tetrahedra (SFT). Material response to neutron irradiation depends in part on its stacking fault energy (SFE). SFE describes the energy that is needed to split a perfect dislocation into two partial dislocations. Materials which have low SFE often exhibit SFT, while the formation of dislocation loops is preferred by the materials with high SFE [1]. However, by only considering the effect of materials SFE on the existence of SFT, experimental results show some inconsistency. For example, SFT are observed in Pd (SFE = 180 mJm^{-2}) and Cu (SFE = 45 mJm^{-2}), but not in Al (SFE = 166 mJm^{-2}) [2]. By introducing a concept of “reduced SFE”, which is the SFE divided by a product of the shear modulus and Burgers vector of a perfect dislocation (SFE / μb), a criteria for the SFT existence can be derived. Namely, materials which have reduced SFE smaller than 1/50 show SFT, while the others form dislocation loops.[2] In the case of copper, the reduced SFE = 1 / 310 [2] and the SFT are thus the predominant irradiation-induced defects (about 90 %) [1].

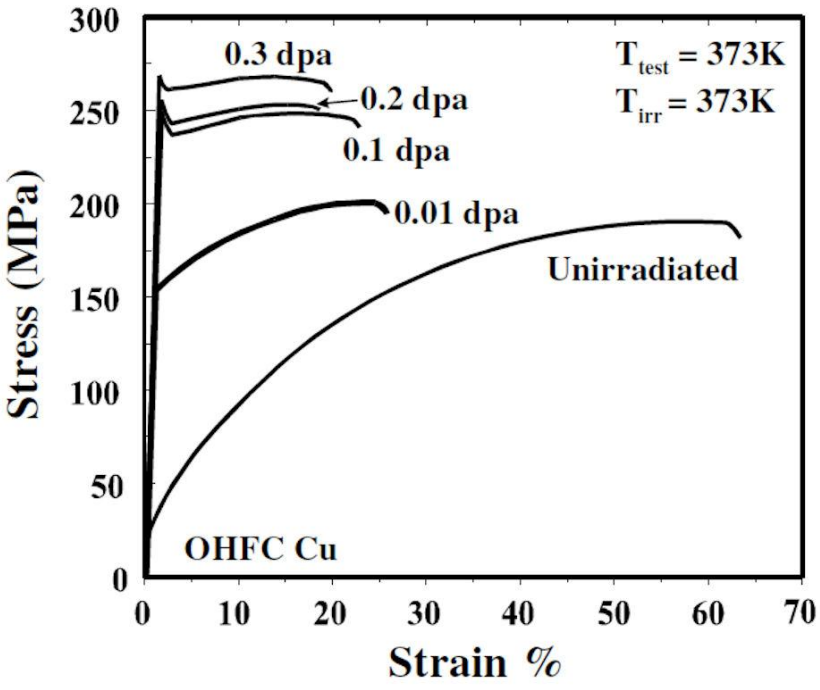

Fig. 1 An example of irradiation-induced hardening of copper.[3]

The early experimental work (as in Fig. 1) has mainly focused on the tensile testing of irradiated samples, e.g., post-irradiation tests. During the last decade dynamic in-reactor tests have shown that the tensile behaviour may change when deformation and neutron irradiation occur simultaneously [4]. When considered from the practical aspects of plant operation or basic materials research, the neutron-dislocation interactions are of particular interest.

The aim of this research was to quantitatively characterize the effects of neutron-irradiation on oxygen-free, high-conductivity (OFHC) copper, and to broaden our expertise in TEM by learning the weak-beam imaging method. Weak beam dark field (WBDF) imaging is a particularly suitable tool for the analysis of the small centers of strain that originate from neutron irradiation (such as dislocation loops, voids, and SFT). The basic physical principles of the WBDF method assure that all the defects are detected within the microscope resolution without any complexity in the contrast formation.

2 Materials and Methods

Four OFHC copper samples were investigated in this study. They had been irradiated at 323 K in the BR-2 reactor at SCK-CEN according to Table 1. The specimens themselves are shown in Fig. 2. The samples were simultaneously tensile tested during neutron-irradiation, using a novel pneumatic testing device placed in the reactor core (see complete description from [4]). Detailed results of the dynamic tensile tests will be reported elsewhere. The main topic of the current study was to identify and determine the density of the SFT.

Table 1 Neutron-irradiation details of the studied samples.

Spec. No.	**Neutron Flux [10^{13} n cm^{-2} s^{-1}]**		**Neutron fluence [10^{18} n cm^{-2}]**		**dpa**	
	E > 0.1 MeV	**E > 1 MeV**	**E > 0.1 MeV**	**E > 0.1 MeV**	**Rate [10^{-8} 1/s]**	**Total [10^{-3}]**
191	3.8	1.7	12.3	5.5	4.3	10.2
193	4.0	1.8	12.8	5.7	4.5	9.8
260	5.3	2.4	32.6	14.5	6.0	37.9
261	3.7	1.6	22.3	9.9	4.1	25.1

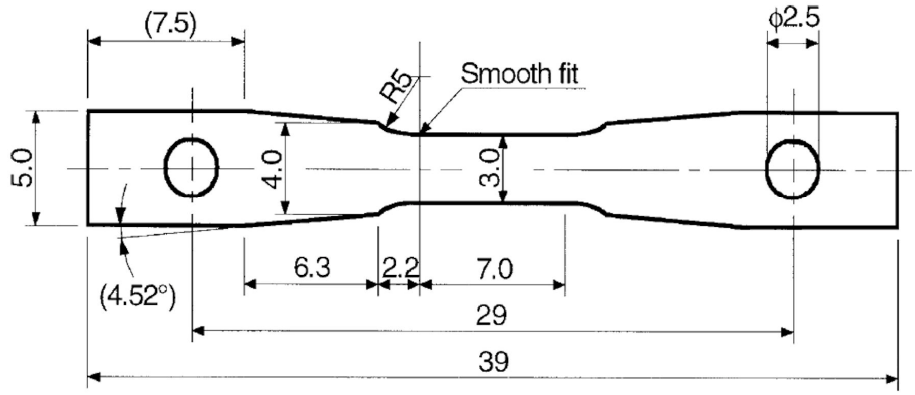

(a)

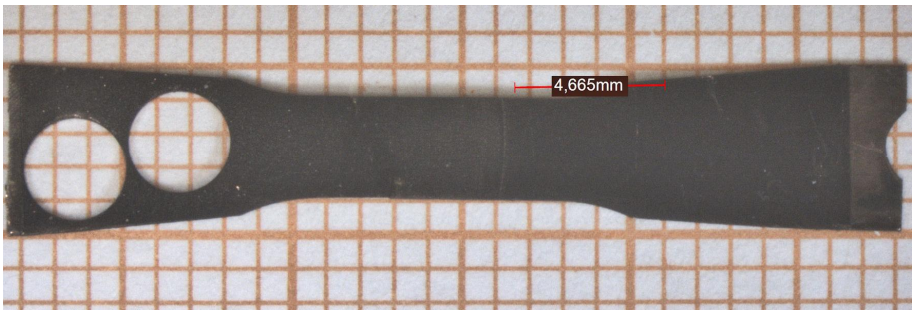

(b)

Fig. 2 (a) Geometry and dimensions of the in-reactor tensile specimens. (b) Stereomicroscope image of sample 261 which shows the position of punched TEM blanks. Notice that the undeformed head sections of the bars were cut off at SCK-CEN before the samples were shipped to VTT. The center regions of the bars were saved for microstructural investigations.

2.1 TEM sample preparation

TEM specimen blanks 3 mm in diameter were punched from the 0.3 mm thick tensile test bars and then manually ground to the thickness of 0.1 mm. The specimens were then electropolished to electron transparency by using phosphoric acid –based Struers electrolyte D2 at room temperature, with a bias voltage ranging from 12 to 14 V (~200 mA). Previously a HNO_3 -based electrolyte had been used for polishing of copper specimens [5] but in the present case it became clear that the HNO_3 was too aggressive an acid for polishing purpose. As a comparison, Fig. 3 (a) and (b) show scanning electron microscopy (SEM) observations of TEM-ready samples that have been prepared by using either the HNO_3 –based electrolyte or the D2 electrolyte, respectively. Clear marks of etching are visible in the sample made with HNO_3, while that made with D2 was of good quality. It was also concluded from the SEM observations, in agreement with previous experiences, that the gray portions inside the bright edge region were electron transparent, and thus appropriate for TEM examination.

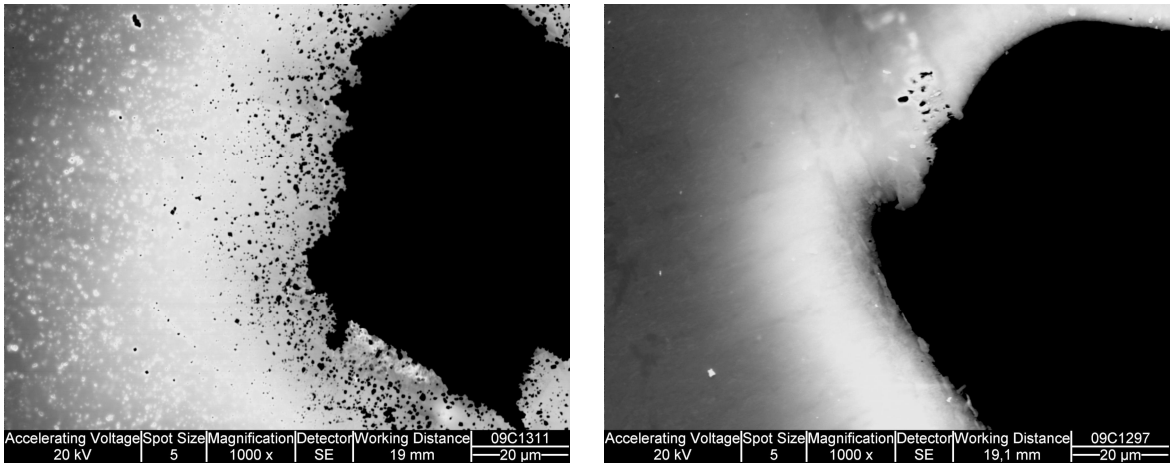

(a) (b)

Fig. 3 SEM of copper TEM test samples fabricated by using (a) the HNO_3 –based electrolyte or (b) the Struers D2 electrolyte, which is H_3PO_4 based.

A problem from the use of the D2 electrolyte was also revealed though, namely that surface contamination of the specimens was a severe problem throughout the work. To reduce the surface contamination, several post-process procedures were tested. The procedures included combinations of rinsing the samples in acetic acid [6], citric acid [7], hot and cold water, ethanol, methanol, and the electrolyte D2. As a conclusion it was determined that the best sample quality was obtained by rinsing the samples first in distilled water, then in ethanol, followed by blow drying. However, it was also determined that future copper specimens should be prepared and investigated on the same day, to minimize the evolution of surface contamination. Further, the electrolyte should be changed frequently to assure good specimen quality.

2.2 Weak beam dark field method

WBDF was used to identify and quantify the amount of irradiation-induced SFT in copper. The main principles of the WBDF method are given below. Detailed description of the method can be found from, for example, [8]. Irradiation-induced defects, e.g. small centers of strain, are problematic to investigate by any method. These defects show complex contrast variation (or no contrast at all) under conventional 2-beam imaging conditions. The advantages of using WBDF include non-dynamic contrast formation and improved contrast as compared to the 2-beam techniques in TEM. However, even though the contrast is good, the image intensity in WBDF is low, which leads to long exposure times and blurred images if the sample is drifting. Focusing the low-intensity image is also challenging.

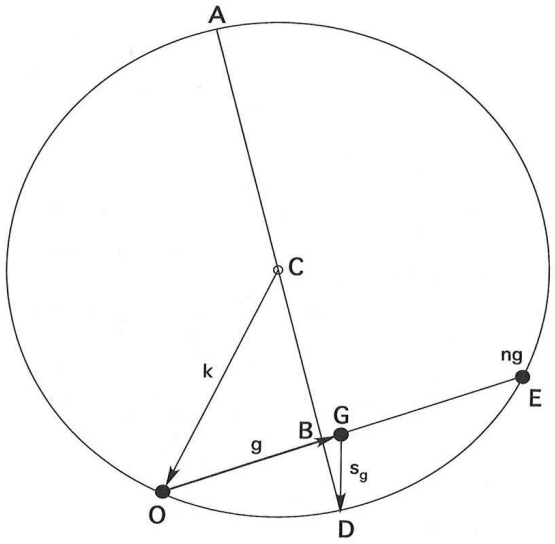

*Fig. 4 (**g**,n**g**) weak beam dark field imaging conditions. $\mathbf{s}_g$ is the deviation from the exact Bragg condition at G, while **s** = 0 at n**g**. The momentum of the incoming electron beam (**k**) defines the Ewald sphere, and **g** is the diffraction vector. Letters A, B, C, D, E,G and O are used for geometric considerations in* [8]

WBDF imaging is based on setting a higher order reflection (n**g**) into an exact Bragg condition, and then using the first order diffraction spot (**g**) to form the dark field image. The notation for the described situation is (**g**,n**g**). The easiest way to visualize the condition is by considering the event in reciprocal (momentum) space, as shown in Fig. 4. The Ewald sphere is determined by the momentum (**k**) of the incoming electron beam. Since each point on this sphere will satisfy the Bragg rule, it can be seen that point E, a vector n**g** away from O, satisfies the rule. The distance from point G to the Ewald sphere is the deviation ($\mathbf{s}_g$) from the exact Bragg condition at G. The WBDF image is made by selecting the diffraction spot at **g** (point G), which is $\mathbf{s}_g$ away from the Bragg condition. With a large $\mathbf{s}_g$, only defects (small centers of strain) can bend the crystal lattice back into the Bragg condition and give well localised contrast to the image. Even though the overall image intensity is low in WBDF, the visibility of defects is much better than in dynamical or kinematical conditions.

The imaging conditions are defined by the value of $\mathbf{s}_g$.

- If $\mathbf{s}_g = 0$, then the condition is dynamical, and the small irradiation-induced features show complex contrast. Quantitative analysis usually requires computer simulations.
- If $0 < \mathbf{s}_g < 0.2 \times 10^{-1}$ nm^{-1}, the condition is kinematical. The small defects lose their complex contrast and enable a more reliable estimate of the number of defects. The image intensity is good and the condition can be used when ultimate resolution is not needed.
- If $\mathbf{s}_g > 0.2 \times 10^{-1}$ nm^{-1}, the “weak beam criteria” is filled. The small defects show well localized and plain contrast. The best quantitative analysis can be done by using this condition.

The exact value for $\mathbf{s}_g$ can be determined from a diffraction pattern that shows diffraction spots and Kikuchi lines. According to [7], the n at (**g**,n**g**) notation can be derived from equation (1):

$$n = 2m - N, \tag{1}$$

where m and N are, respectively, the distances (divided by |**g**|) of a certain Kikuchi line (for example +2) and a certain diffraction spot N (spot 2 in this case) from the transmitted beam. The value for $\mathbf{s}_g$ can then be calculated from equation (2):

$$s_g = \frac{1}{2}(n-1)|g|^2 \lambda. \tag{2}$$

When a thin area of TEM sample is investigated at high magnification, it is evident that the image intensity oscillates from bright to dark when the foil thickness increases. These thickness fringes can be used to give an estimate of the sample thickness, because each oscillation from bright to dark corresponds to half of the extinction distance. An obvious advantage for using WBDF for thickness determination can be understood by examining equation (3):

$$\xi = \frac{1}{s_{eff}} = \frac{1}{\sqrt{s_g{}^2 + \frac{1}{\xi_g^2} +}}, \tag{3}$$

where $\mathbf{s_g}$ is the deviation from Bragg condition as previously, and ζ_g is the tabulated extinction distance for a given reflection **g**. When $\mathbf{s_g}$ increases, the extinction distance decreases and more fringes for the same thickness variation are produced as compared to the 2-beam case (where $\mathbf{s_g} = 0$, $\zeta = \zeta_g$).

As an example, one fringe spacing in Cu in dynamical two-beam conditions with **g** = 200 at 200 kV, originates from a thickness variation of one electron extinction distance of 35.6 nm. For comparison, by using (**g**,5**g**) WBDF conditions, one spacing of fringes corresponds to 6.4 nm, which creates about six times more fringes for the same thickness variation, and therefore more accurate estimation of the sample thickness than the 2-beam condition. As an example of experimental WBDF thickness determination, shows the effect of increasing the value of $\mathbf{s}_g$ from the dynamical two beam conditions of (a) to the weak beam conditions of (c) via the kinematical conditions of (b).

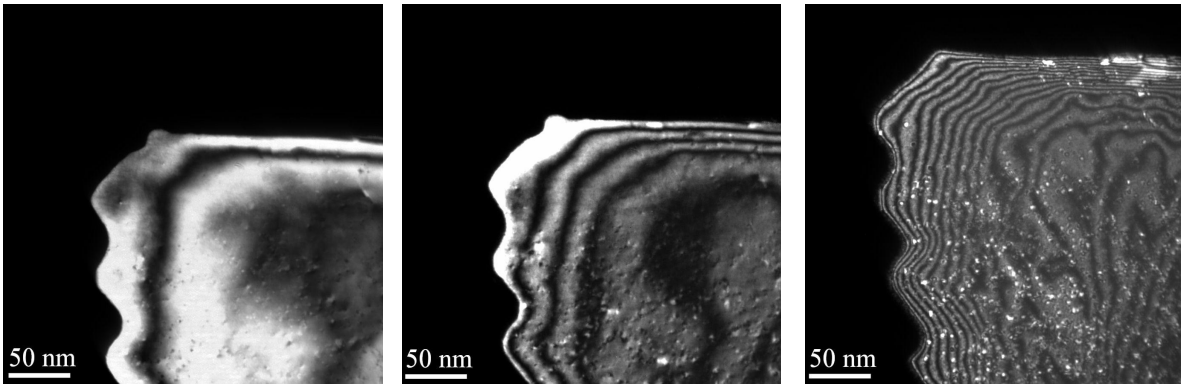

(a) (b) (c)

Fig. 5. (a) dynamical (s_g =0), (b)kinematical ($\mathbf{s}_g$ > 0), and (c) weak beam dark field conditions ($\mathbf{s}_g$ >0.2 × 10^{-1} nm^{-1}).

Another advantage of using WBDF for the thickness determination is the ability to evaluate thicknesses that are much less than the tabulated dynamical extinction distance ζ_g. For example, the minimum thickness for the convergent electron beam diffraction (CBED) -based technique at two-beam conditions, is around a couple of ζ_g (~50 nm).

2.3 SFT imaging and quantification

The quantitative analysis of the SFT densities in the materials of this study was done as follows. First, a thin region with a good surface quality was sought out and tilted close to the (100) or (110) pole. Then the foil was slightly tilted off from the exact zone axis and suitable diffraction conditions were set up by tilting the sample, guided by the Kikuchi lines. Sample thickness was determined by calculating the thickness fringes in the WBDF conditions (as explained in section 2.2). Magnifications in the range of 200 kx were used for imaging. A box was placed on the image and the SFT density inside the box was calculated (the box dimensions were obtained directly from the Digital Micrograph software). An example of the actual counting procedure is given below.

In Fig. 6, the WBDF conditions are (**g**, 6**g**) and **g** = (200). The extinction distance for this condition is 5.2 nm. Altogether seven thickness fringes are observed, which totals a sample thickness of 36.4 nm. The white box of Fig. 6 (b) has dimensions of 35 nm × 75 nm. Multiplying these values with the obtained thickness, a total volume of 9.7 × 10^{-23} m^3 is determined. Inside this volume, 41 SFT were found (white circles). Dividing the number of SFT by the obtained volume thus gives an SFT density of 4.3 × 10^{23} SFT/m^3.

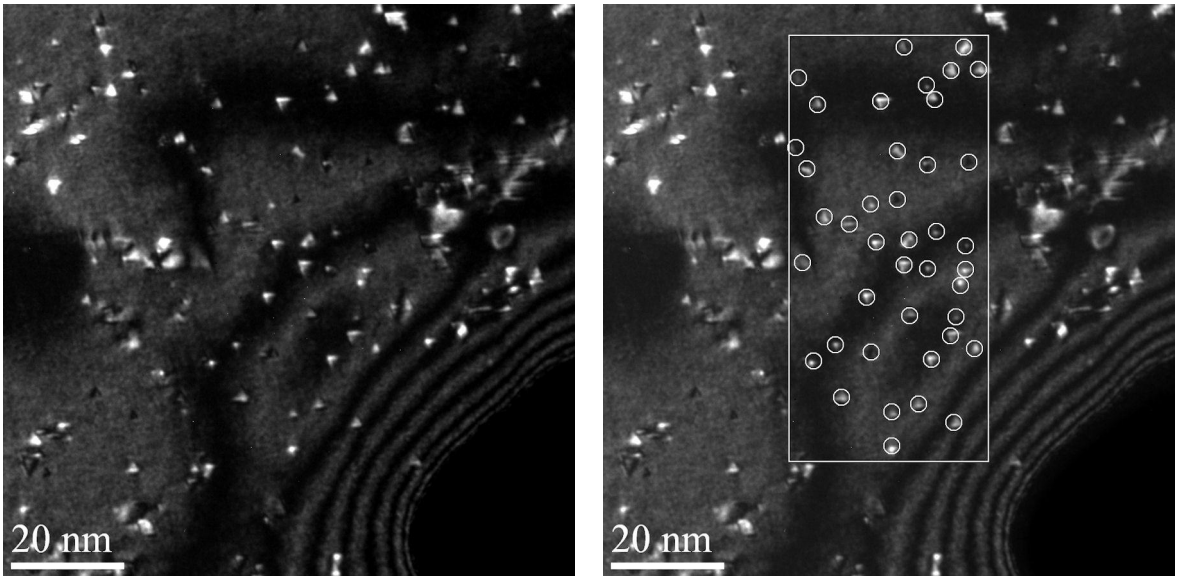

(a) (b)

*Fig. 6 (a) Sample 191 imaged by using (**g**,6**g**) WBDF conditions at **g** = (200). The white box in (b) shows the analyzed region and the white circles are counted as SFT.*

By using the example given above, a brief calculation of possible errors in the obtained SFT density was made. The errors were screened by varying either the sample thickness or the amount of detected SFT by ±20, ±40 or ± 60 %. The results are compiled in Table 2. The error in sample thickness is most likely caused by the error made in the determination of the WBDF condition. On the other hand, the error in the calculation of the amount of SFT originates is likely due to poor resolution and criteria used. Notice that the effect of increased thickness is opposite to the increased amount of SFT.

Table 2. Error estimations due to uncertainty in the determined thickness (upper panel) or in the amount of calculated SFT (lower panel).

Thickness [nm]	Number of SFT	SFT density [10^{23} m^{-3}]
14.6 (- 60 %)	41.0	10.7
21.8 (- 40 %)	41.0	7.2
29.1 (- 20 %)	41.0	5.4
36.4	41.0	4.3
43.7 (+ 20 %)	41.0	3.6
51.0 (+ 40 %)	41.0	3.1
58.2 (+ 60 %)	41.0	2.7
36.4	16 (- 60 %)	1.7
36.4	25 (- 40 %)	2.6
36.4	32 (- 20 %)	3.3
36.4	41	4.3
36.4	49 (+ 20 %)	5.1
36.4	57 (+40 %)	6.0
36.4	66 (+60 %)	6.9

By using the values of Fig. 6 (b) but an erroneous extinction distance of (**g**,5**g**) instead of (**g**,6**g**) produces an error of slightly over 20 % in thickness and a SFT density of 3.5 10^{23} SFT/m^3 (instead of the correct 4.3 × 10^{23} SFT/m^3). Thinking backwards, an error of similar size would need 8 “extra” SFT to be found if the weak beam condition is correctly determined and thus the sample thickness is correct. From experience, the latter seems more unlikely. Based on the error screening test and the example given above, an error limit of ± 1 × 10^{23} SFT / m^3 for the WBDF method seem justified.

3 Results

3.1 Analysis of stacking fault tetrahedra

After finding an appropriate low-contaminated area from the sample surface, the copper specimens were tilted close to the (110) or (001) zone. The nature and visibility of SFT was first explored by taking high-resolution (HR) images without any aperture, and thus without diffraction contrast. Fig. 7 (a) to (d) show (110) down-zone high-resolution observations for the sample 261 (0.025 dpa). In good agreement with the theory and previous results in the literature, the low magnification image in Fig. 7 (a) shows that the sample consists of a large number of small SFT and a relatively small portion (by number) of more complicated features that could be dislocation loops or defects originating from surface contamination. Previously reported ratio of 90 % SFT and 10 % loops (or defect clusters) seems well justified. By increasing the magnification, the nature and shape of the SFT became visible. Notice that in Fig. 7 (b) some surface oxide contribution (“zebra” pattern) is clearly visible at the lower left corner of the image. When studying samples that were stored longer in vacuum, the amount of these oxide features increased dramatically, thus making quantitative SFT determination impossible. By increasing the magnification even more [Fig. 7 (c) and (d)] the triangular SFT became even more clearly detectable. From the HR-images, the SFT size distribution was determined to range from ~1 nm to a bit less than 5 nm, as expected from previous results reported in the literature [9].

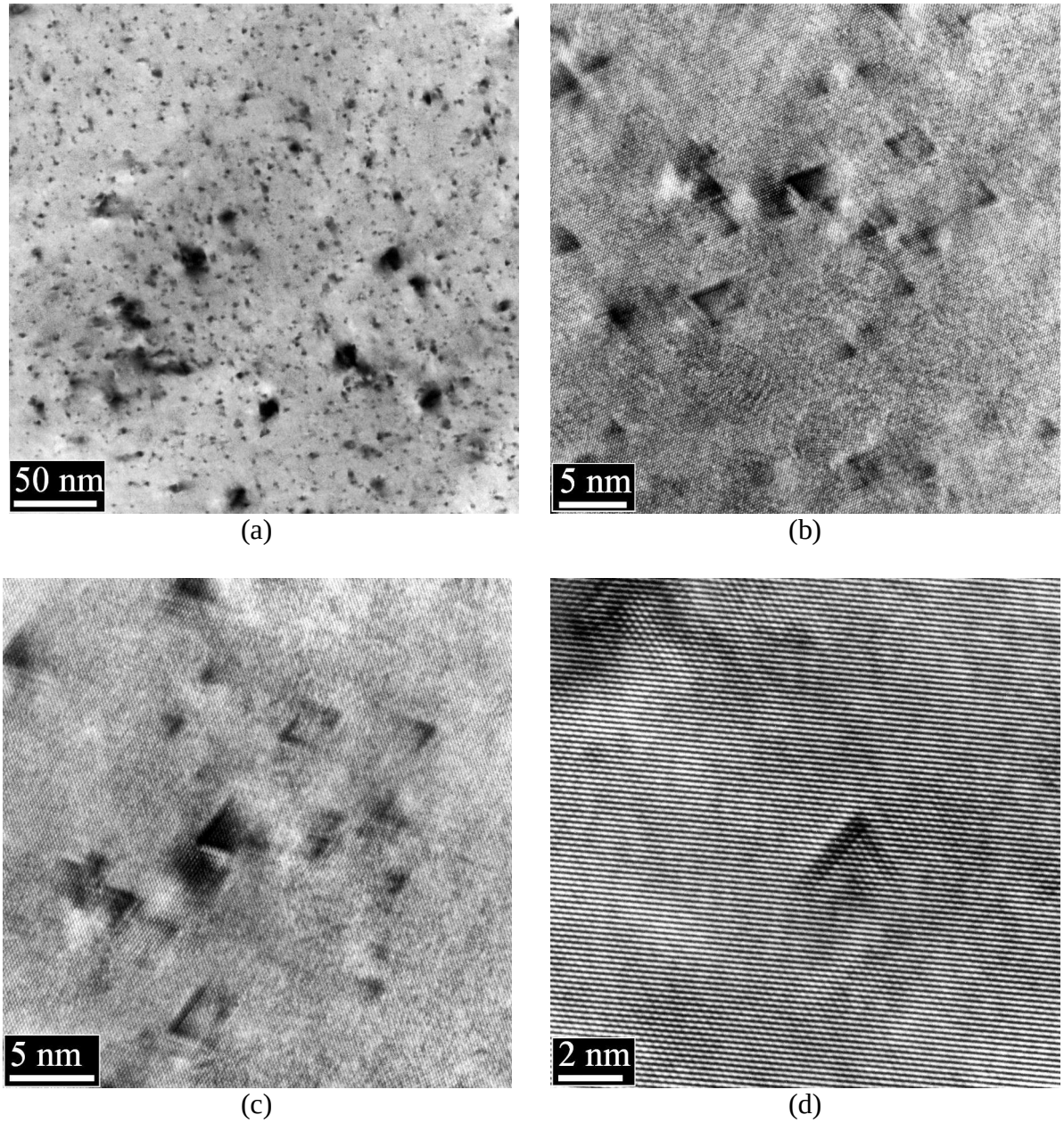

Fig. 7 Down-zone images of sample 261 close to the (110) pole. A set of SFT are displayed in (c), while in (d) one SFT is shown with a high magnification.

By using the Kikuchi diffraction pattern, the samples were tilted to suitable WBDF conditions. Upon finding the zone of interest [(110) or (001)], the sample was tilted a couple of degrees off from the axis to minimize the excitation of non-systematic reflections. The weakly excited dark field diffraction spot at **g** = 200 was centered at the optical axis of the microscope (point G in Fig. 4) and used for imaging. The diffraction pattern obtained was also simulated by using Web Electron Microscopy Applications Software (WebEMAPS) to confirm the WBDF conditions [10]. An example of an experimental and simulated diffraction pattern pair is shown in Fig. 8.

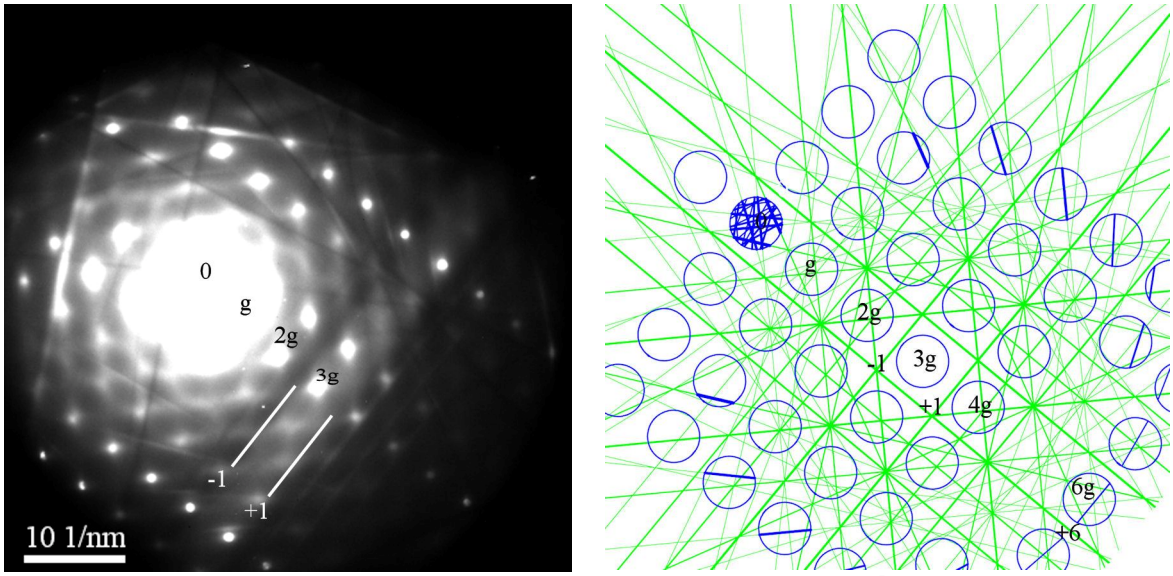

(a) (b)

*Fig. 8 Experimental (a) and simulated (b) diffraction patterns for (**g**,6.2**g**) WBDF conditions close to the (100) pole. Notice that the sixth Kikuchi line is a bit over the sixth diffraction spot and therefore the exact Bragg condition was found to be (**g**,6.2**g**). All the diffraction spots (for example 5**g**) are not shown due to limitations of the calculations. The simulation was done by using WebEMAPS* [10].

From the study of experimental and simulated diffraction patterns, a method for setting the desired WBDF conditions was developed. It very quickly became clear, as is also shown in Fig. 8 (a), that the diffraction condition cannot be easily seen by examining the (**g**,n**g**) spot that is in exact Bragg orientation. However the bright line intersecting the diffraction spot 3**g** in Fig. 8 (a), is always more easily found. The position of bright line immediately defines the diffraction condition, because it shows the position of the -1 and +1 Kikuchi lines [the distance between two Kikuchi lines (excluding the "0" line) is half of **g,** and the exact Bragg condition is met when the same Kikuchi line and diffraction spot intersect].

Fig. 9 shows example WBDF images for each of the four samples of this study. Throughout the images, the copper matrix shows variation of contrast from bright to dark. This variation is due to surface roughness. Notice that the small effective extinction distance is an advantage of WBDF when determining sample thickness but a disadvantage when the sample has a lot of local thickness variation. In the (**g**,~6**g**) conditions with **g** = (002), SFT are visible as white triangles.
A direct comparison of SFT densities in Fig. 9 (a) to (d) is not possible though, since the local foil thicknesses are different in each case.

In the SFT density calculations, all resolvable features were counted as SFT whether they clearly showed triangular shape or not. The contribution of truncated SFT, dislocation loops, and raft-like dislocation segments on SFT density determination is discussed in the next section. The obtained results are summarized in Table 3.

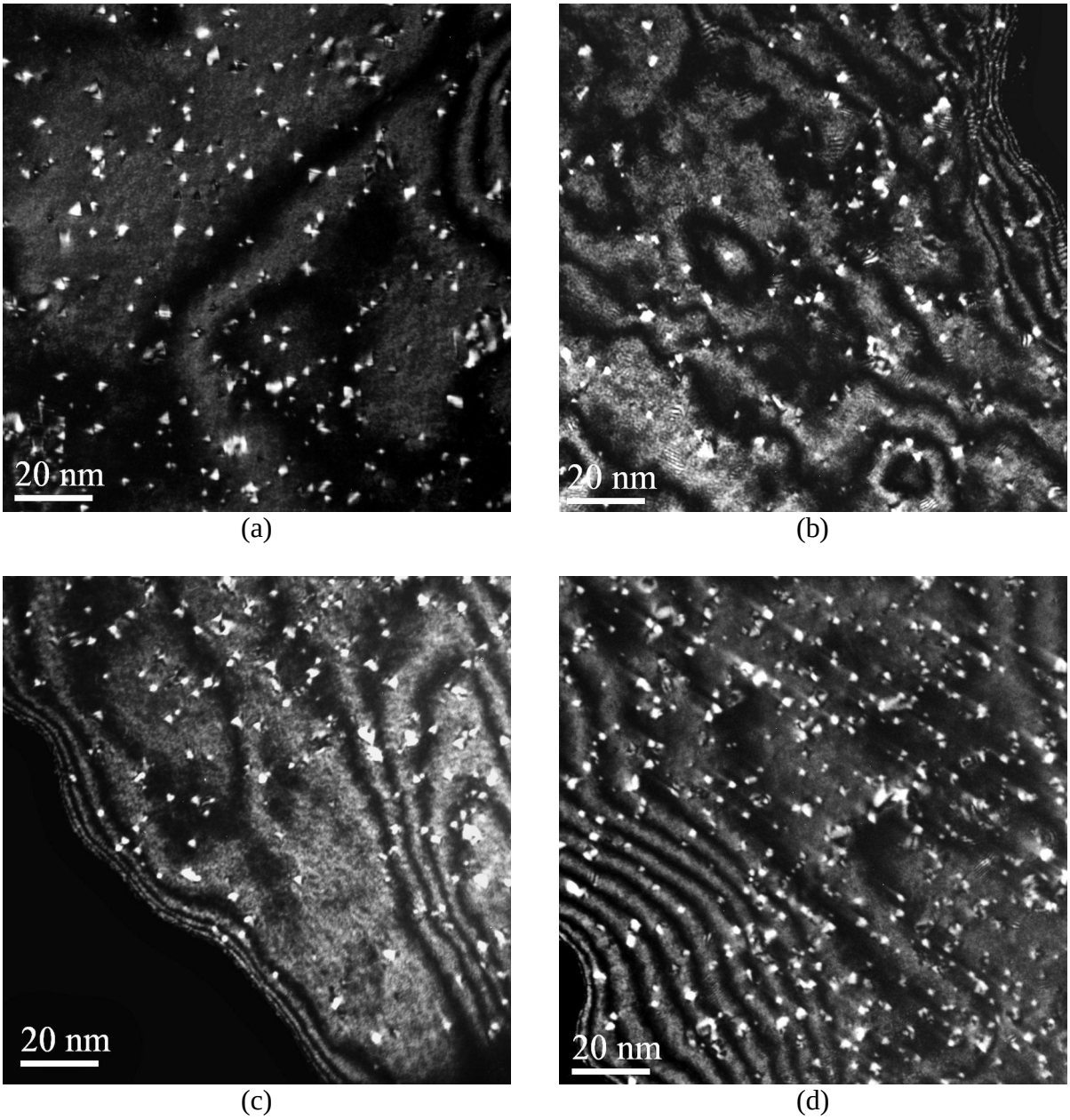

*Fig. 9 Samples (a)191, (b) 193, (c) 260, and (d) 261 imagined by using WBDF conditions (**g** = 200). The SFT have triangular shape. Notice that sample thickness increases the apparent SFT density, while poor surface quality accompanied by microstructural defects reduces the image quality.*

Table 3. The obtained SFT densities.

Sample	Dose (dpa)	SFT density (10^{23} SFT/m^3)
Bar 191	10.2	3.6
Bar 193	9.8	3.7
Bar 260	37.9	4.5
Bar 261	25.1	5.2

4 Discussion

A set of results from earlier neutron irradiation experiments of copper and the results obtained in this work are compared in Fig. 10. As can be seen, the SFT density values are quite scattered. Upon increasing the dose, the SFT density saturates close to a value of 1 (± 2) × 10^{24} SFT/m^3. When comparing to [11], in which the irradiation parameters are nearly identical to this work, slightly higher SFT density was obtained in this work. Taking into account the error estimation done in Section 2.3, the values are, however, within the error limits of ± 1 × 10^{23} SFT/m^3.

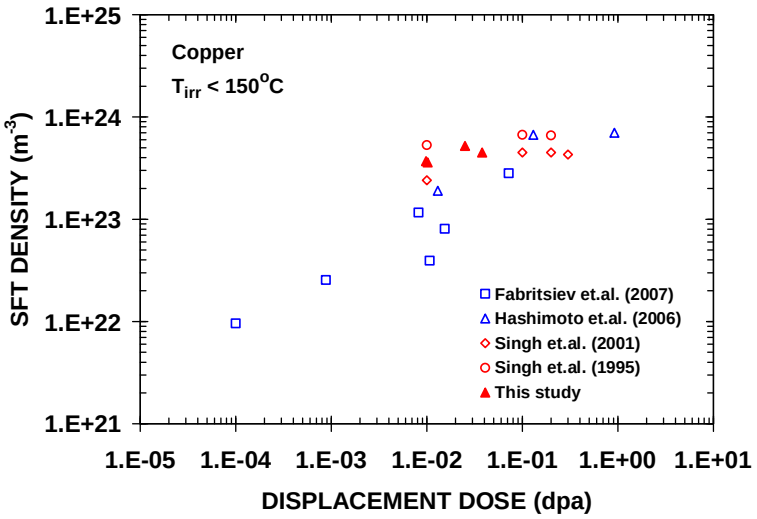

Fig. 10 A comparison between SFT densities observed in this work and previous results from literature. See articles [11-14] *for details.*

Surface quality plays a critical role in quantitative TEM analysis [8]. The uneven oxidation of electro polished copper surfaces is a known fact. The effect of the surface quality can be clearly seen in Fig. 9. The best surface with the lowest amount of contamination and thickness variation [Fig. 9 (a)] has a smooth, bright to dark contrast variation, and clearly triangular and resolvable SFT. The other images [Fig. 9 (b), (c), and (d)] also show similar SFT but suffer from diverse contrast and somewhat poorer resolution.

While surface finish can be optimized by careful specimen preparation, microstructural effects may also contribute to the quantitative SFT density measurement result. In Fig. 11, a loop-like feature A is imagined first by using dynamical 2 beam conditions and then by using (**g**,3**g**) conditions. What resembles a loop in Fig. 11 (a) looks like a set of defects arranged in a circular shape in Fig. 11 (b). The same applies for the features in Fig 11 (a) and (b) labeled B and C; defects that produce dark, loop-like contrast in dynamic 2-beam conditions tend to consist of small, separate segments in (**g**,3**g**) conditions. Whether these segments are pinned by SFT and should be included when determining the SFT density or not remains an unanswered question. The effect of these features clearly increases the SFT density if they are included. As a conclusion, it is clear that all extra features, often originating from other microstructure or surface finish effects, can easily degrade the resolution below that needed for the most accurate quantitative SFT analysis. In the literature, in

addition to the SFT density, often a density for dislocation loops or defect clusters is given. When examining the microstructure of Fig. 11 (a) SFT are clearly the dominant irradiation defects. The density of the defect clusters is substantially lower than the one of SFT.

Nonetheless, the values calculated for SFT density in this study were in line with those found in literature. The increasing density of SFT upon increasing the irradiation dose further gives justification for the applied WBDF method, which included the SFT calculation from a representative area and the thickness determination by using thickness fringes at weak beam conditions.

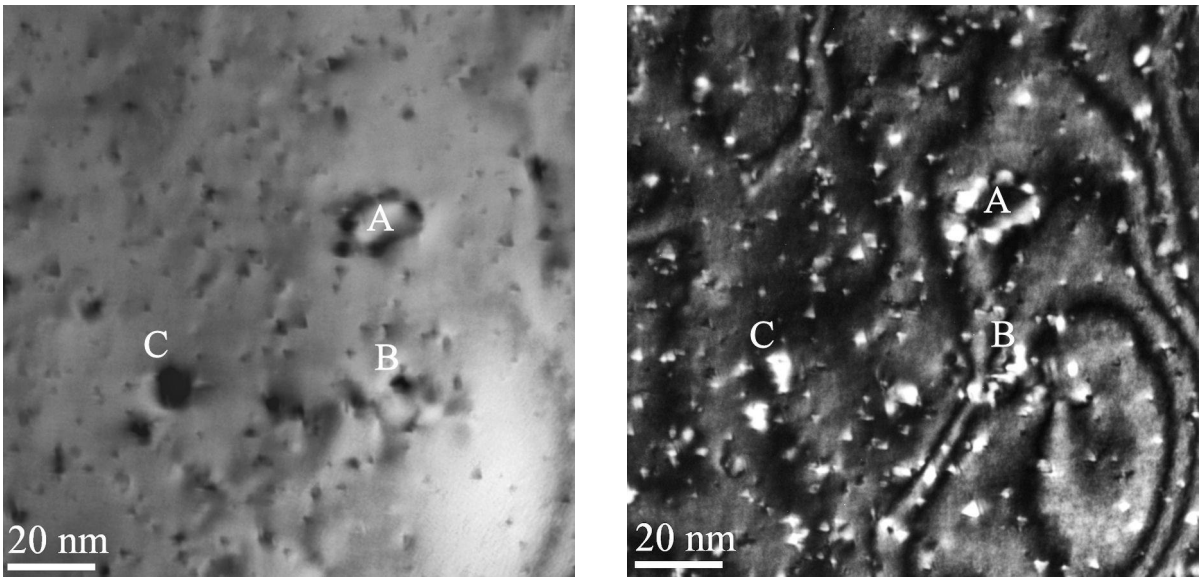

(a) (b)

*Fig. 11 (a) Dynamical 2 beam and (b) (**g**,3**g**) observation of SFT and other types of defects. Labeled features from A to C show same positions on each image.*

5 Conclusions

Through this study the WBDF imaging method was learned and successfully employed for the quantitative analysis of the defect density of four different neutron irradiated copper specimens. The size and type of the SFT was determined based on HRTEM imaging, and was found to correspond to the findings of previous experiments reported in the literature. It was found that the neutron irradiation doses from 0.001 to 0.040 dpa produced SFT densities from 3.6 to 5.2 $\times 10^{23}$ SFT/m^3. The effects of microstructural defects and surface finish on SFT density determination were discussed.

6 References

[1] T.D. de la Rubia, H.M. Zbib, T.A. Khraishi, B.D. Wirth, M. Victoria, and M.J. Caturla, Multiscale modelling of plastic flow localization in irradiated materials, Nature. 406 (2000) 871-874.

[2] R. Schäublin, Z. Yao, N. Baluc, and M. Victoria, Irradiation-induced stacking fault tetrahedra in fcc metals, Phil. Mag. 85 (2005) 769 - 777.

[3] D.J. Edwards, B.N. Singh, and J. Bildesorensen, Initiation and propagation of cleared channels in neutron-irradiated pure copper and a precipitation hardened CuCrZr alloy, J. Nucl. Mater. 342 (2005) 164 - 178.

[4] B.N. Singh, S. Tähtinen, P. Moilanen, P. Jacquet, and J. Dekeyser, In-reactor uniaxial tensile testing of pure copper at a constant strain rate at 90 °C, J. Nucl. Mater. 320 (2003) 299-304.

[5] W. Karlsen and J. Pakarinen. , TEM microstructures of copper following three different EAC tests, Espoo, VTT Research Report VTT-R-08100-09, 2009.

[6] K.L. Chavez and D.W. Hess, A Novel Method of Etching Copper Oxide Using Acetic Acid, J. Electrochem. Soc. 148 (2001) G640 - G643.

[7] E. Hoppe, A. Seifert, C. Aalseth, P. Bachelor, A. Day, D. Edwards, T. Hossbach, K. Litke, J. McIntyre, and H. Miley, Cleaning and passivation of copper surfaces to remove surface radioactivity and prevent oxide formation, Nucl. Instrum. Meth. A. 579 (2007) 486 - 489.

[8] M.L. Jenkins and M.A. Kirk, Charachterization of Radiation Damage by Transmission Electron Microscopy, Institure of Physics Publishing, London, 2001.

[9] B.D. Wirth, V.V. Bulatov, and T.D. de la Rubia, Dislocation-Stacking Fault Tetrahedron Interactions in Cu, J. Eng. Mater. Technol. 124 (2002) 329 - 334.

[10] J.M. Zuo and J.C. Mabon, Web-Based Electron Microscopy Application Software: Web-EMAPS. 10 (2004) 1001.

[11] B.N. Singh, D.J. Edwards, and P. Toft, Effect of neutron irradiation and post-irradiation annealing on microstructure and mechanical properties of OFHC-copper, J. Nucl. Mater. 299 (2001) 205-218.

[12] S. Fabritsiev and A.S. Pokrovsky, Effect of irradiation temperature on microstructure, radiation hardening and embrittlement of pure copper and copper-based alloy, J. Nucl. Mater. 367-370 (2007) 977 - 983.

[13] N. Hashimoto, T.S. Byun, and K. Farrel, Microstructural analysis of deformation in neutron-irradiated fcc materials, J. Nucl. Mater. 351 (2006) 295 - 302.

[14] B.N. Singh, A. Horsewell, P. Toft, and D. Edwards, Temperature and dose dependencies of microstructure and hardness of neutron irradiated OFHC copper, J. Nucl. Mater. 224 (1995) 131-140.